# Comparison of the Electronic Structures of $VX_3$ (X = Br, and I) using High-resolution X-ray Scattering

Chamini S. Pathiraja, Deniz Wong, Christian Schulz, Yi-De Chuang, Yu-Cheng Shao, and Byron Freelon Physics Department and Texas Center for Superconductivity, University of Houston, Houston, TX 77204

Helmholtz-Zentrum Berlin für Materialien und Energie, D-14109 Berlin, Germany

Lawrence Berkeley National Laboratory, Berkeley, CA 94720

Antional Synchrotron Radiation Research Center,

101 Hsin-Ann Road, Hsinchu Science Park, Hsinchu, Taiwan 30076

(Dated: November 25, 2025)

## Abstract

Transition-metal halides  $VX_3$  (X=Br and I) have emerged as promising candidates for two dimensional spintronic and quantum applications due to their layer-dependent magnetism and tunable electronic states. However, experimental insights into their ground state electronic structures remain limited. Here, we present a comprehensive investigation of  $VX_3$  using high resolution resonant inelastic x-ray scattering (RIXS) combined with ligand field multiplet calculations. The RIXS spectra reveal distinct dd and charge-transfer excitations, allowing precise determination of electronic structure parameters, including the crystal field splitting, trigonal distortion, and Racah parameters. The determined parameters showed clear variation, indicating an increase in covalency from Br to I. The trigonal distortion parameters  $\Delta_{D_{3d}}$  were determined to be -0.096 eV in VBr<sub>3</sub> and 0.07 eV in VI<sub>3</sub>, indicating a sign opposition between the two compounds, reflecting good agreement with experimental RIXS data. Cluster model calculations yield a high-spin  $V^{3+}$  (S=1) configuration, with an  $e_3'^2$  ground state in VBr<sub>3</sub> and an  $e_3'^4$  argument of the previously conflicting theoretical reports and confirm that VBr<sub>3</sub> is an insulator while VI<sub>3</sub> exhibits Mott insulating behavior induced by spin-orbit coupling. Our findings provide the most complete experimental determination of the low energy electronic structure in VX<sub>3</sub>, offering valuable insights for designing 2D magnetic and spintronic materials based on vanadium halides.

### I. INTRODUCTION

Two-dimensional (2D) materials have attracted intense research interest since the discovery of Graphene, owing to their unique electronic and magnetic properties. Among them, transition metal (TM) trihalides with a honeycomb arrangement in the metal ions have emerged as particularly promising systems. Chromium trihalides  $\operatorname{Cr} X_3$  ( $X=\operatorname{Cl}$ , Br, and I) with S=3/2 are well studied and are notable for sustaining long-range magnetic order down to the monolayer limit, with their properties strongly dependent on dimensionality, halogen chemistry, interlayer interactions, and temperature [1–4].

Recently, theoretical predictions and experiments have extended this interest to the vanadium trihalides VX<sub>3</sub> (X = Br and I) with S = 1 [5–8]. These compounds undergo structural phase transitions from high-temperature monoclinic to low-temperature rhombohedral phase at 90 K (VBr<sub>3</sub>) and 79 K (VI<sub>3</sub>), similar to CrX<sub>3</sub> [9–11]. Subsequent magnetic phase transitions have been reported, where VBr<sub>3</sub> enters an antiferromagnetic (AFM) phase at 29.5 K, while VI<sub>3</sub> exhibits ferromagnetic (FM) order below 50 K [9, 10, 12].

 ${
m V}X_3$  are layered van der Waals materials with a honeycomb lattice of  ${
m V}^{3+}$  cations, each coordinated by six halogen anions in edge-sharing octahedra (see Figure 1(a-b)). In a perfect octahedral crystal field with  $O_h$  symmetry, the V 3d orbitals split into two energy levels  $t_{2g}$  and  $e_g$ . However, the partial filling of the  $t_{2g}$  orbitals in  ${
m V}X_3$  introduces Jahn-Teller (JT) distortions by splitting the  $t_{2g}$  orbital into  $a_{1g}$  and  $e'_g$ , lowering its symmetry from  $O_h$  to the trigonal  $D_{3d}$  (see Figure 1(c)) [8, 13, 14]. This

distortion can produce unquenched orbital moment and single ion anisotropy via  $V^{3+}$  spin-orbit coupling (SOC) in contrast to  $CrX_3$ , where anisotropy arises mainly from exchange interactions mediated by halogen orbitals [15].

Despite intensive study, the detailed crystal structure and electronic properties remain controversial. Two types of JT distortion in  $VX_3$  have been proposed in the literature: (Type I) trigonal compression, yielding a ground state with half occupied  $e'_g$  state and fully occupied  $a_{1g}$  orbital  $(e'_g^1 a_{1g}^1)$ , and (Type II) trigonal elongation, where the  $e'_g$  state is fully occupied  $(e'_g^2)$  [7, 16, 17]. These configurations correspond to distinct electronic behavior, where the half-occupied state typically results in metallicity, while the fully occupied configuration opens an insulating gap. There are conflicting reports about the ground state electronic configurations in both VBr<sub>3</sub> and VI<sub>3</sub>, and hence the metallic or insulating nature [6, 7, 9, 11, 16, 18, 19].

Theoretical studies also suggested that including SOC in density functional theory calculations can open additional splitting in the  $e_g'$  manifold with a reasonable Coulomb interaction U, stabilizing an insulating state with a small optical band gap in  $e_g'^1 a_{1g}^1$  state which considered to be metallic otherwise [7, 8, 16]. This insulating state is argued to be stabilized by Mott correlation effects rather than JT distortion [7, 11, 19]. Thus, while both theoretical and experimental evidence point to complex interplay among crystal-field, SOC, and correlation effects, a comprehensive experimental determination of the ground-state electronic configuration in  $VX_3$  and, hence the elongation/compression remains elusive.

Although the metallic or insulating nature in  $VX_3$  may

not solely depend on the local crystal field of  $V^{3+}$  ion, precise knowledge of the crystal field splitting parameters is paramount. This will guide the determination of ground state orbital configuration in  $VX_3$ . Understanding the electronic state near the Fermi level is crucial for unraveling the origin of magnetism in these compounds. Obtaining accurate energy scales is therefore a necessary step toward constructing robust theoretical models of the magnetic ground states in  $VX_3$ .

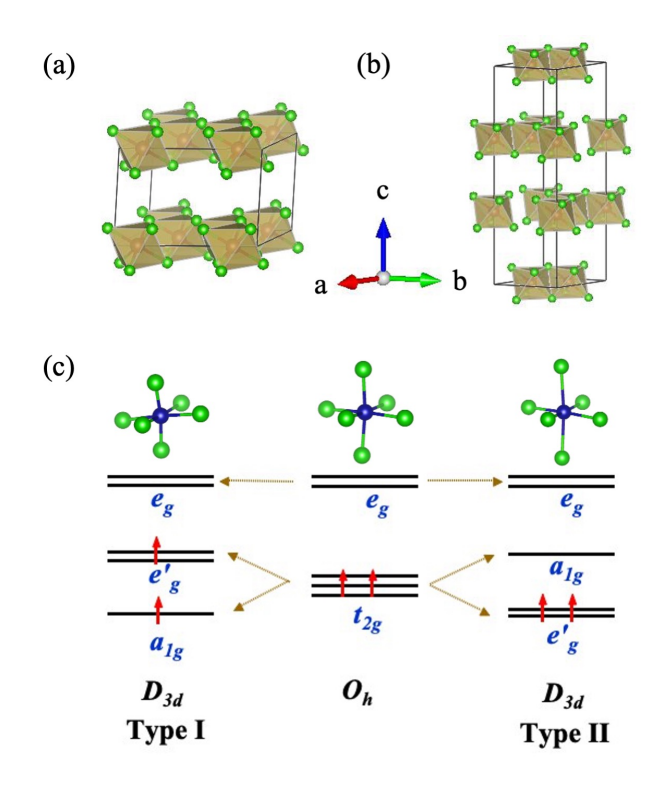


FIG. 1. (a) crystal structure of  $VX_3$  in monoclinic and (b) rhombohedral structure (c) Crystal field splitting of the V 3d orbitals when the symmetry is lowered from  $O_h$  to  $D_{3d}$  symmetry. The Type I (II) configuration corresponds to the trigonal compression in  $VX_3$  as shown in the  $VX_6$  cluster unit.

X-ray scattering techniques provide a powerful means of probing the electronic structure of TM-based structures and complexes. The development of synchrotron sources has enabled x-ray photon energies that directly match the relevant electronic transitions in many TMs. Resonant inelastic x-ray scattering (RIXS), in particular, is a  $photon - in \ photon - out$  spectroscopy that allows the study of the momentum, energy, and polarization changes of the scattered photon [20]. In particular, the soft x-rays (0.1–2.0 keV) can excite TM 2p electrons into unoccupied valence orbitals at the TM L-edge, making RIXS particularly suited to probe dd excitations and charge-transfer (CT) excitations in 3d or 4d TM complexes. [20–22].

In this work, we report the first high-resolution RIXS measurements of  $VBr_3$  and  $VI_3$ . The experimental spec-

tra, combined with atomic multiplet calculations, provide direct evidence of the ground state electronic configuration and detailed electronic structure parameters in  $VX_3$ . The calculated energy level diagrams (ELDs) are compared with experimental RIXS spectra to optimize the energy scales. Our results identify an  $e_g^2$  (trigonal elongation) ground state in VBr<sub>3</sub> and an  $e_g'^1a_{1g}^1$  (trigonal compression) ground state in VI<sub>3</sub>, consistent with prior theoretical predictions, providing a comprehensive experimental foundation for understanding the electronic and magnetic properties of  $VX_3$ .

#### II. EXPERIMENT METHOD

 $VX_3$  single crystals were obtained from HQ Graphene (Groningen, Netherlands). Due to the samples' high hygroscopicity and sensitivity to oxygen, the  $VX_3$  samples were stored and handled under an inert gas (Ar) atmosphere in a glovebox environment to minimize air exposure. The samples were subjected to scotch tape exfoliation before being transferred to the experimental chamber to ensure a clean surface. The experimental chamber was maintained in dark conditions and at a high vacuum (5 × 10<sup>-9</sup> Torr) during the measurements.

The preliminary  $VX_3$   $L_{2,3}$  XAS measurements and RIXS measurements were obtained at the qRIXS end station, beamline 8.0.1 at the Advanced Light Source, Lawrence Berkeley National Laboratory, with a resolution of 0.3 eV [23]. High-resolution XAS and RIXS data were collected at the PEAXIS beamline at BESSY II, Germany, with a resolution of 80 meV [24].

The data were collected at four different temperatures: 14, 65, 100, and 300 K, and three different incident angles: 20, 50, and 90 degrees with respect to the sample surface. At all experimental conditions, the x-ray photon beam was horizontally polarized to the scattering plane ( $\pi$ -polarization). The crystalline c-axis was aligned within the scattering plane. The spectrometer for RIXS was kept at  $140^0$  (back scattering geometry). An opencycle cryostat with liquid nitrogen (LN<sub>2</sub>) flow was used to cool down the VX<sub>3</sub> samples to low temperatures.

# III. RESULTS

# A. V L edge XAS measurements

Figure 2 presents the V L edge XAS data collected for VBr<sub>3</sub> and VI<sub>3</sub>. The dipole allowed electronic transition  $(2p^63d^2 \rightarrow 2p^53d^3)$  gives rise to two broad structures in the 510-520 and 520-530 eV regions, which can be attributed as the  $L_3(2p_{J=3/2})$  and  $L_2(2p_{J=1/2})$  edges, respectively. The  $L_3$ -edge peak maxima occur at 515.5 eV for VBr<sub>3</sub> and 514.9 eV for VI<sub>3</sub>, showing a clear decrease in energy as the halogen changes from Br to I. This trend is consistent with previous observations in Cr $X_3$  compounds [21, 25].

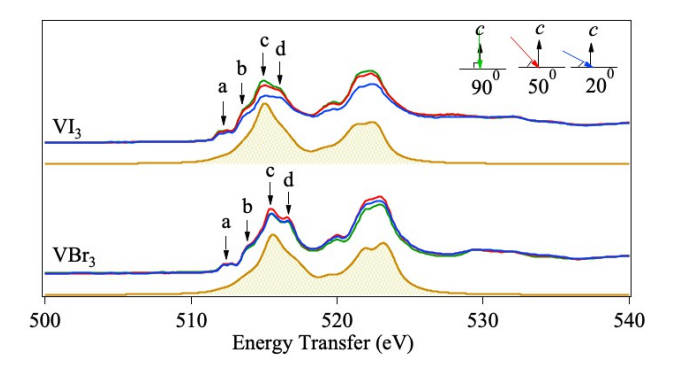


FIG. 2. V L edge XAS data in VBr<sub>3</sub> and VI<sub>3</sub> at different x-ray incident geometries. The blue, red, and green lines indicate the XAS data collected at  $20^{\circ}$ ,  $50^{\circ}$ , and  $90^{\circ}$  with respect to the sample surface (see the top right schematic diagram). The yellow shaded spectra show the simulated XAS spectra at 300 K

The penetration of an x-ray beam depends on the refractive index of the material and the incident angle [26]. The XAS spectra were collected at different incident angles;  $20^{\circ}$ ,  $50^{\circ}$ , and  $90^{\circ}$  relative to the sample surface, as indicated by the blue, red, and green lines in figure 2. The grazing incidence geometry  $(20^0)$  primarily probes the surface region, while normal incidence  $(90^{\circ})$ probes deeper into the bulk. A pronounced intensity variation with the angle was observed in VI<sub>3</sub>, consistent with the depth-dependent sensitivity described above. In contrast, VBr<sub>3</sub> exhibited a weaker angular dependence, possibly due to surface oxidation effects that alter nearsurface electronic states. It is also worth noting that grazing incidence geometry enhances in-plane electronic excitations, whereas the normal incidence predominantly probes out-of-plane electronic excitations.

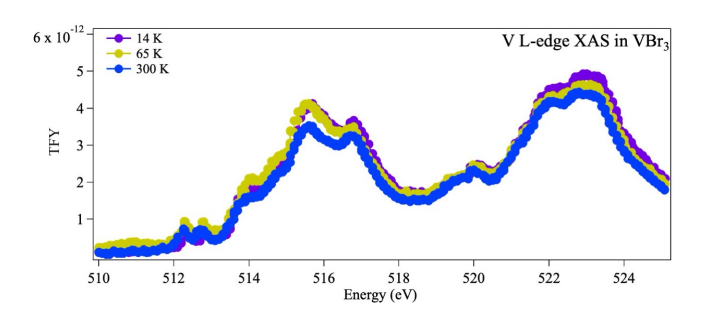


FIG. 3. Temperature dependent V L- edge XAS data in VBr<sub>3</sub>. The purple, yellow, and blue lines show the data collected at 14, 65, and 300 K, respectively. All the data were measured at the normal incidence geometry.

Figure 3 shows the temperature dependent V L-edge XAS spectra of VBr $_3$  measured at 14 K, 65 K, and 300 K, spanning over the structural and magnetic phase transition temperatures. While no significant energy shift was observed upon cooling to 14 K, slight intensity variations were observed. The 300 K XAS spectrum shows a dis-

tinct intensity redistribution compared to the 14 K and 65 K spectra. This indicates a clear relationship to the different structures at given temperatures, as  $VX_3$  is in the monoclinic structure at 14 K and 65 K, and the trigonal structure at 300 K. However, the energy changes in the XAS spectra for a given material are subtle at the three temperatures, indicating that the local environment surrounding V near the sample surface has only undergone subtle changes. A similar behavior was reported in  $VO_2$  [27].

## B. V $L_3$ -edge RIXS measurements

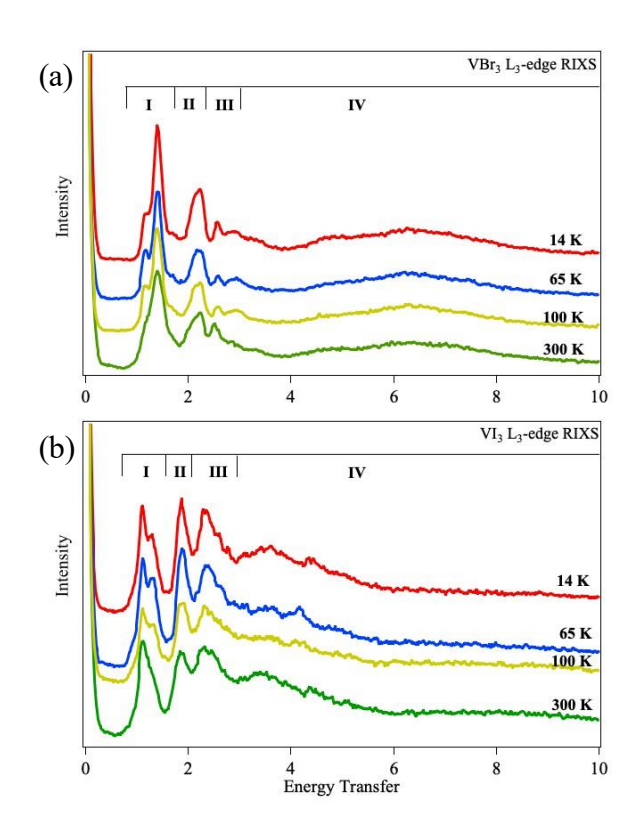


FIG. 4. a) Temperature dependence RIXS measurements in VBr<sub>3</sub> and b) VI<sub>3</sub> at normal incidence. The regions I, II, III, and IV are labeled to show different spectral features in  $VX_3$ .

Although the XAS provides valuable insight into key electronic excitations, its finite spectral broadening can complicate the precise determination of energy scales. On the other hand, it has been demonstrated that RIXS can provide more detailed information about electronic structure parameters with greater precision due to the sharpening effect in RIXS that bypasses core-hole lifetime broadening [20, 21]. Figure 4 presents the V  $L_3$ -edge RIXS spectra of V $X_3$ , measured at the excitation energy 'c' across different temperatures: 14, 65, 100, and 300 K. All the data were measured when the incident photon beam is normal to the sample surface.

Four main energy transfer regions (I - IV) are identified

in the RIXS spectra. The regions I, II, and III can be attributed to the inter-orbital dd excitations, while region IV represents broader CT excitations. In region I, VBr<sub>3</sub> exhibits a low-energy shoulder feature, whereas VI<sub>3</sub> indicates a shoulder feature on the high-energy side. The primary peak maxima in region I were observed at 1.4 eV (VBr<sub>3</sub>)and 1.1 eV (VI<sub>3</sub>), revealing a shift towards lower energy as the halogen changes from Br to I. The peak intensity in region III also changes significantly between the two compounds, consistent with the optical measurements [28]. Covalent bonds in VBr<sub>3</sub> have well-separated dd excitations and CT excitations, while the ionic bonds in VI<sub>3</sub> indicate a possible overlapping of CT excitations with the dd excitations, resulting in this intensity variation over the compounds.

The temperature-dependent spectra correspond to different crystallographic phases: rhombohedral at 14 K and 65 K, and monoclinic at 100 K and 300 K. Both compounds are magnetically ordered at 14 K. Despite these phase and magnetic transitions in  $VX_3$ , no substantial peak shifts are observed upon cooling, implying that the local environment around vanadium remains largely unchanged. However, the intensity of the shoulder features in regions I and III evolves with temperature, indicating a clear relation between the magnetic states and low energy excitations in  $VX_3$ .

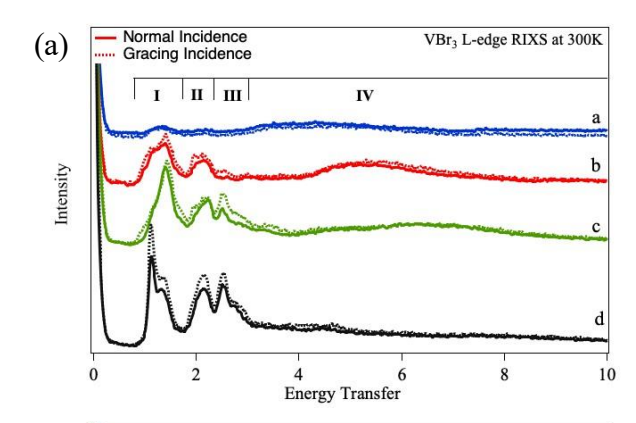
RIXS spectra obtained in the soft x-ray regime exhibit a clear incident and final photon energy dependence. Figure 5 shows the RIXS spectra of VBr<sub>3</sub> and VI<sub>3</sub> collected at different excitation energies at room temperature 300 K. While the CT features shift with the incident energy, the dd excitations showed only subtle changes, though their intensities vary markedly. The dominant peak in region I has high intensity at the  $L_3$ -edge, while the shoulder features gain relatively high intensities as the excitation energy moves away from the  $L_3$  peak.

The dashed lines in Figure 5 indicate the RIXS spectra collected at the grazing incidence, and they only show a subtle energy shift in the spectral features compared to the normal incidence. However, the grazing incidence RIXS spectra show higher intensity, contrary to the XAS intensity.

# IV. $VX_6$ CLUSTER CALCULATIONS

To assign the spectral features in the XAS and RIXS spectra, the atomic multiple calculations were performed to simulate the RIXS spectra using a quantum many-body script language Quanty [29, 30]. The large V-X covalency necessitates the consideration of charge-transfer effects, including the  $3d^2$  and  $3d^3L$  electronic configurations in the calculations, where L corresponds to a hole in the ligand orbitals (I 5p). The ligand field Hamiltonian was expressed as,

$$H = H_{Coulomb} + H_{SOC} + H_{CFT} + H_{LMCT} + H_{Exchange}$$
(1)



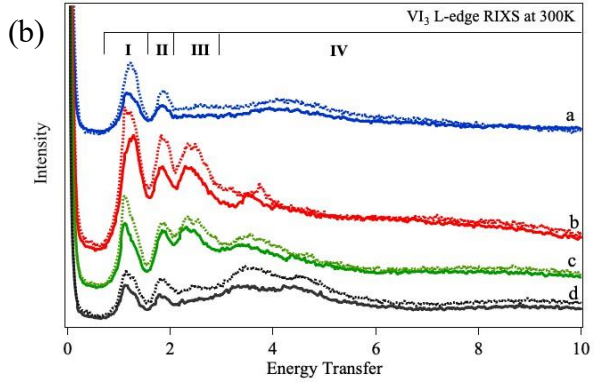


FIG. 5. a) Excitation energy dependence RIXS measurements in  $VBr_3$  and b)  $VI_3$  at 300 K. The solid and dashed lines indicate the normal incidence and grazing incidence, respectively. The excitation energies a, b, c, and d are as labeled in Figure 2

This includes the interorbital Coulomb interaction effect  $(H_{Coulomb})$ , crystal field effect  $(H_{SOC})$ , spin-orbit coupling  $(H_{SOC})$ , the ligand to metal charge transfer effect  $(H_{LMCT})$ , and exchange Heisenberg interaction effect  $(H_{Exchange})$  [29–32].

The electronic Hamiltonian in Quanty was then solved using second quantization to calculate the RIXS spectra and ELDs. The relevant electronic configurations of  $2p^63d^2$  and  $2p^53d^3$  in the ground state and the excited state resulted in the atomic multiplets  ${}^3F < {}^1D < {}^3P < {}^1G < {}^1S$ . These multiplets can be described by 3d-3d Coulomb and 2p-3d exchange interactions parameterized in Slater-Condon integrals  $F^k_{dd}$ ,  $F^k_{pd}$  (Coulomb), and  $G^k_{pd}$  (Exchange) for Hatree-Fock calculations [29, 33]. They can be related to the Racah B and C by,

Racah 
$$B = (9F_{dd}^2 - 5F_{dd}^4)/441$$
  
Racah  $C = 5F_{dd}^4/63$  (2)

to account for the ion covalency [34].

Initial starting parameters for the multiplet calculations were obtained from the references, and the standard notations [7, 16, 35, 36]. The Hubbard  $U_{dd}$  of 3.82 eV (VBr<sub>3</sub>) and 2.91 eV (VI<sub>3</sub>) was used in the simulations,

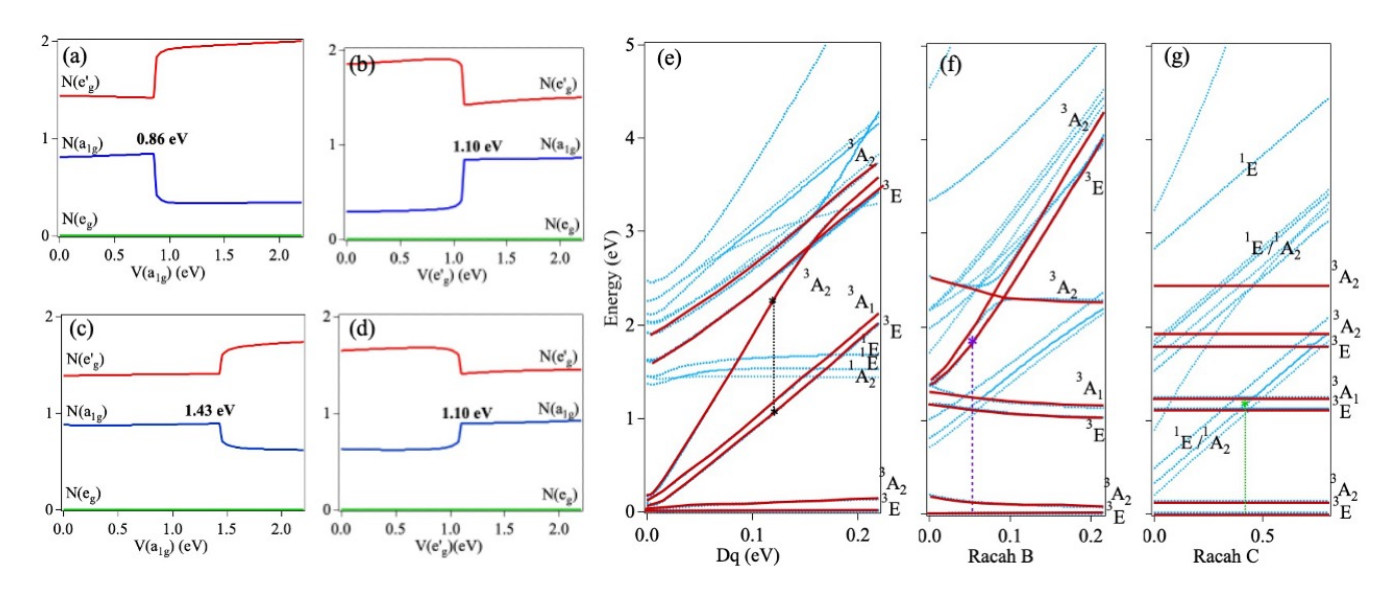


FIG. 6. (a)-(b) Calculated orbital occupations of the  $e_g$  (green)  $a_{1g}$  (blue) and  $e'_g$  (red) states per V atom as function of the symmetry adapted potentials  $V(a_{1g})$  and  $V(e'_g)$  in VBr<sub>3</sub> and (c)-(d) in VI<sub>3</sub> (e) Energy level diagrams as a function of crystal field Dq (f) Racah B and (g) Racah C in VI<sub>3</sub>. The triplet and singlet states in V<sup>+3</sup> metal are shown by solid red and dashed blue lines, respectively.

while the ratio of  $U_{dd}/U_{pd}$  was kept constant at 1.43 [7]. The charge transfer energy ( $\Delta$ ) was kept as 3.30 and 3.00 eV in VBr<sub>3</sub> and VI<sub>3</sub>, following the same trend as CrX<sub>3</sub> [7, 25]. The V 3d SOC was selected to be 13 meV following Lane et al., which corresponds to the 50% of the atomic value [37, 38]. The crystal field splitting in VX<sub>3</sub> and the trigonal distortion is discussed in Appendix A.

### A. Electron occupation and hybridization

As the ligand hybridization affects the excited energy states significantly, the hybridization parameters were determined through a detailed calculation of electronic occupations in each  $e_g$ ,  $a_{1g}$ , and  $e_g'$  orbital. Figure 6 (a)-(b) shows the calculated electron occupancy results as a function of the hybridization parameters  $V(a_{1g}$  and  $V(e_g')$  in VBr<sub>3</sub> and (c)-(d)VI<sub>3</sub>. In each panel, the number of electrons was counted in each orbital  $e_g$  (green),  $a_{1g}$  (blue), and  $e_g'$  (red). There was no electron count in the  $e_g$  orbital, and it remained constant. The electron count in  $e_g'$  and  $e_g'$  and  $e_g'$  states is mainly related to the V  $e_g'$  orbital or I) ions, and they varied symmetrically as a function of  $e_g'$  and  $e_g'$  and  $e_g'$  and  $e_g'$  and  $e_g'$  and they varied symmetrically as a function of  $e_g'$  and  $e_g'$  a

From Figure 6, the  $V(a_{1g})$  was determined to be 0.86 eV and 0.86 eV for VBr<sub>3</sub> and VI<sub>3</sub>, respectively, while  $V(e_g')$  was 1.10 eV in both halide systems. The hopping integral  $V(e_g)$  was kept constant at 1.7 eV in all calculations following Sant et al. as they report a similar discussion of the electron occupation calculation, and are in close agreement with our values [7]. The ELDs also showed a high dependency on the hopping integrals  $V(a_{1g}), V(e_g')$ , and  $V(e_g)$ , and determining them through

electron occupation was more accurate and consistent with other studies.

# B. Determination of electronic structure parameters

After determining the initial parameters, the ELDs were computed to extract key electronic structure parameters, crystal field splitting parameter 10Dq, Racah B, and Racah C, as shown in Figures 6(e)-(g). The reported ELDs correspond to VI<sub>3</sub>; however, similar calculations for VBr<sub>3</sub> were performed and are not presented here for brevity. In Figures 6(e)-(g), the dashed blue and solid red lines represent the spin-singlet and spin-triplet states, respectively. Each state is labeled by the term symbol corresponding to  $D_{3d}$  symmetry.

Under an  $O_h$  crystal field with  $e_g$  and  $t_{2g}$  orbitals, the atomic triplet states split into the manifolds:  ${}^3F \to {}^3A_{2g}$ ,  ${}^3T_{2g}$ , and  ${}^3T_{1g}(1)$ , and  ${}^3P \to {}^3T_{1g}(2)$ . The JT distortion under  $D_{3d}$  symmetry further splits the  $t_{2g}$  orbitals into  $a_{1g}$  and  $e'_g$  states, producing branching transitions such as;  ${}^3T_{2g} \to {}^3A_1 \times {}^3E$  and  ${}^3T_{1g} \to {}^3A_2 \times {}^3E$  [39]. The splitting of these multielectronic atomic states depends on the trigonal distortion parameter  $\Delta_{D_{3d}}$  as discussed in appendix A [21].

Figure 6(e) shows the ELD depicting the evolution of multielectronic energy states as a function of Dq. The crystal field splitting parameter 10Dq was determined from the electronic transition  $^3A_2 \rightarrow ^3E$  states (marked line), corresponding to the first and third peak observed in the experimental RIXS spectra [39]. The extracted 10Dq values are 1.370 eV for VBr<sub>3</sub> and 1.220 eV for VI<sub>3</sub>,

TABLE I. Summary of the energy scales calculated for  $VX_3$  using multiplet ligand field theory calculations (all energies are in eV).

	VBr <sub>3</sub>		$VI_3$	
	$(2p^63d^2)$	$(2p^53d^3)$	$(2p^63d^2)$	$(2p^53d^3)$
$U_{dd}$	3.820	3.820	2.910	2.910
$U_{pd}$	5.463	5.463	4.161	4.161
10Dq	1.370	1.370	1.220	1.220
$\Delta_{D_{3d}}$	- 0.096	- 0.096	0.070	0.070
$\operatorname{Racah} B$	0.057	0.069	0.050	0.061
Racah $C$	0.423	0.459	0.423	0.459
$F_{dd}^2$	5.754	6.588	5.411	6.200
$F_{dd}^4$	5.330	5.778	5.330	5.778
$F_{pd}^2$ $G_{pd}^1$	-	5.451	-	4.846
$G_{pd}^1$	-	3.733	-	3.075
$\dot{G}_3^3$	-	2.496	-	2.496
SOC(3d)	0.013	0.018	0.013	0.018
SOC(2p)	-	4.650	-	4.650
$J_H$	0.792	0.792	0.767	0.767
$\mathrm{E}(e_g)$	0.822	0.822	0.732	0.732
$\mathrm{E}(a_{1g})$	- 0.356	- 0.356	- 0.628	- 0.628
$\mathrm{E}(e_g')$	- 0.644	- 0.644	- 0.418	- 0.418

demonstrating a reduction in crystal field strength as the halogen changes from Br to I, consistent with trends in ligand-induced crystal fields [21, 40, 41].

The Racah B parameter, representing interelectronic repulsion, was determined to be 0.057 eV and 0.050 eV for VBr<sub>3</sub> and VI<sub>3</sub>, respectively (see figure 6(f)), indicating an increase in covalency from Br to I [41, 42]. ELDs were also evaluated as a function of Racah parameter C, which predominantly influences singlet-state energies (see Figure 6(g)). The triplet states appear nearly horizontal with increasing C, whereas the singlet states that are associated with spin-flip electronic transitions show clear dependency on Racah C. Optimal fits between the calculated and experimental RIXS spectra were obtained with Racah C = 0.423 eV for both halide systems.

The exchange parameters  $F_{pd}^2$ ,  $G_{pd}^1$ , and  $G_{pd}^3$  were refined by fitting the XAS experimental data as shown in the yellow shaded line in Figure 2; as the RIXS process consists of an XAS process followed by a resonant x-ray emission. The vanadium 2p SOC of 4.65 eV is consistent with the observed energy gap between  $L_3$  and  $L_2$  edges, and in good agreement with literature [38]. All the determined electronic structure parameters are summarized in the table I.

#### C. Simulation of RIXS spectra

After optimizing all the electronic structure parameters, the RIXS spectra were calculated for VBr<sub>3</sub> and VI<sub>3</sub> as shown in Figure 7. Panels (a) and (b) show the calculated RIXS maps for VI<sub>3</sub> and VBr<sub>3</sub>, along with the multiplet energy levels. The calculation of RIXS spectra was only performed at 300 K, as no considerable temperature

dependency was observed in the RIXS spectral features. We find excellent agreement between the two datasets, including the energies of all Raman-like excitations in the RIXS profile and their incident-energy dependence.

The integrated RIXS spectra at the V  $L_3$ -edge in VBr<sub>3</sub> (top) and VI<sub>3</sub> (bottom) are shown in Figure 7(c). The black line shows the experimental RIXS spectra, while the yellow shaded spectra show the calculated RIXS spectra. The spectral features have been labeled with spin-allowed triplet states (red) and spin-forbidden singlet states (blue), respectively. The triplet states  ${}^3A_1$  and  ${}^3E$  showed an ordering of  ${}^3A_1 > {}^3E$  in VBr<sub>3</sub>, while it is switched to  ${}^3E > {}^3A_1$  in VI<sub>3</sub>. This is consistent with the sign opposition in the trigonal distortion parameter  $\Delta_{D_{3d}}$  between VBr<sub>3</sub> (-0.096 eV) and VI<sub>3</sub> (0.070 eV). Note that the CT excitations are not captured in our calculations.

The incidence energy dependence of the experimental RIXS data in Figure 5 can be explained using the spin-forbidden singlet states which were attributed to the shoulder peaks. These singlet states are highly dependent on the SOC; as the inclusion of SOC was necessary to produce the spin-forbidden singlet states. Therefore, the temperature dependency of the RIXS intensity in shoulder features (see Figure 4) can be directly related to the magnetic states in  $VX_3$ . Similar behavior was observed in other TM complexes, ruby,  $CrX_3$ , and Vanadium oxides [21, 33]

#### V. DISCUSSION

From the cluster calculations, a spin moment of  $2 \mu_B$  per V atom was obtained, indicating a high-spin state in V<sup>3+</sup> with S=1. This result is in excellent agreement with the expected value, and aligns well with theoretical predictions of approximately  $2.2-2.6 \mu_B$  per V [9, 11]. The Hund's exchange coupling  $J_H=(F_{dd}^2+F_{dd}^4)/14$  was determined to be 0.792 (VBr<sub>3</sub>) and 0.767 eV (VI<sub>3</sub>), confirming the high-spin state in both compounds, and consistent with the relation  $2J_H<10Dq$  [43]. Literature reports a  $J_H$  of 0.8-0.9 eV in both VX<sub>3</sub>, showing excellent agreement with our results [8, 16, 37, 44]. Through this study, we experimentally determined the ground state electronic configuration of VX<sub>3</sub>. The energies of the  $e_g$ ,  $a_{1g}$ , and  $e'_g$  states are summarized in Table I and are graphically shown in Figure 7(d).

From the calculations, the VBr<sub>3</sub> exhibits a ground state of  $e_g'^2$ , consistent with the Type II configuration characterized by a trigonal elongation (see Figure 1(c)) [14]. The full occupancy of the  $e_g'$  orbitals and empty  $a_{1g}$  orbitals introduces a clear energy gap between the two orbitals, resulting in an insulating state. First principal calculations also suggest an  $e_g'^2$  ground state in VBr<sub>3</sub>, consistent with its reported semiconducting behavior, showing excellent agreement with our findings [5, 8]. The energy gap between the  $E(e_g)$  and  $E(a_{1g})$  is determined to be 1.178 eV and the energy gap between  $E(a_{1g})$  and  $E(e_g')$ 

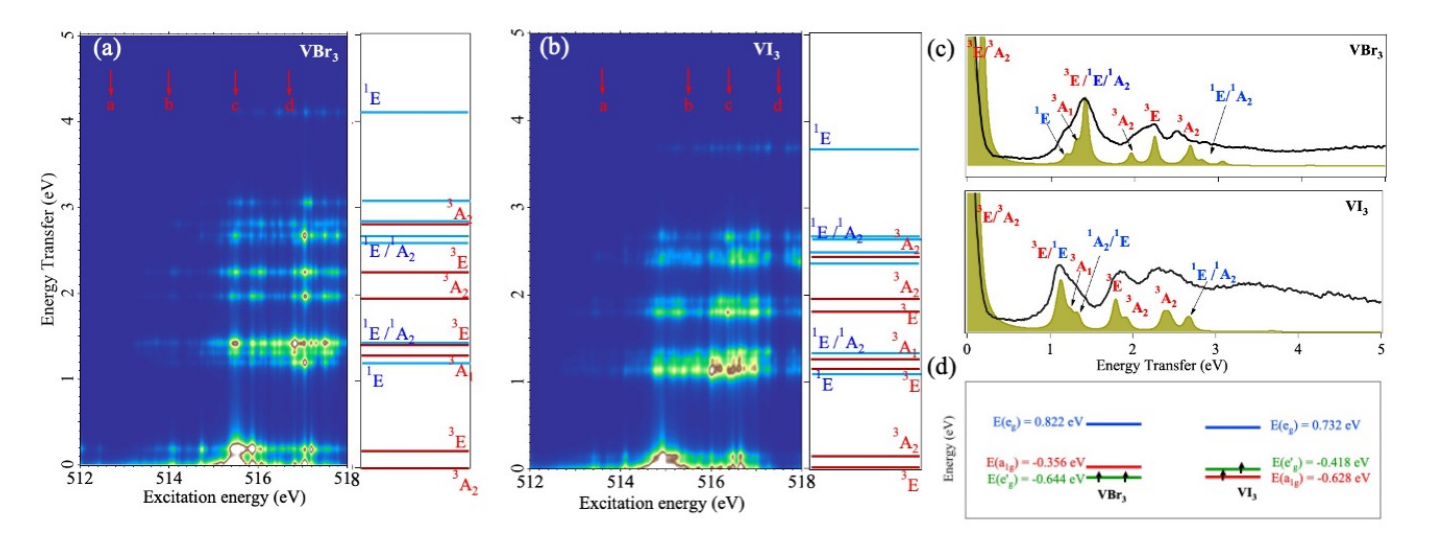


FIG. 7. (a) Calculated RIXS map in VBr<sub>3</sub> and (b) VI<sub>3</sub>. The multiplet energy states are shown next to the RIXS maps. (c) Integrated RIXS spectra calculated at the V  $L_3$ -edge (excitation energy 'c') in VBr<sub>3</sub> (top) and VI<sub>3</sub> (bottom). The black line shows the experimental RIXS spectra, while the yellow shaded spectra show the calculated RIXS spectra. The multielectronic atomic states, singlets and triplets, are labeled in blue and red, respectively. (d) Calculated crystal field splitting orbital energies in VX<sub>3</sub>.

which was determined to be 0.288 eV, is responsible for opening a narrow bandgap, resulting in the insulating state in VBr<sub>3</sub>, showing good agreement with the literature [8].

In contrast to VBr<sub>3</sub>, we determined a  $e_g^{\prime 1} a_{1g}^1$  ground state in VI<sub>3</sub>, consistent with the Type I which corresponds to a trigonal compression as shown in Figure 1(c) [7, 14]. Similar ground state configurations have been reported by Yang et al. and Sant et al. [7, 16]. Although this ground state with partial occupancy in  $e'_q$  orbital leads to a metallic state in nature, it is also reported that the V 3d SOC plays a significant role, and with a reasonable Coulomb interaction U, a splitting of the two  $e_g^\prime$  orbitals can be observed, introducing an insulating state in VI<sub>3</sub> [16]. In particular, Zhao et al. reports bandgap opening of 12.7 meV upon including the SOC in VI<sub>3</sub>, which is consistent with the V 3d SOC from our multiplet calculations [18]. Another report indicates a bandgap of 38.7 meV, and this elevation in SOC was due to the strong I 5p-V 3d hybridization along with the Coulomb interaction U [11, 19].

From the multiplet calculations and the crystal field parameters, we determined that the primary factor governing the distinct ground state configurations in VX<sub>3</sub> is the trigonal distortion parameter  $\Delta_{D_{3d}}$ . The ground state configuration is highly sensitive to both the sign and the magnitude of the  $\Delta_{D_{3d}}$ : a negative  $\Delta_{D_{3d}}$  in VBr<sub>3</sub> leads to an orbital doublet ground state  $(e_g'^2)$ , whereas a positive  $\Delta_{D_{3d}}$  in VI<sub>3</sub> stabilizes an orbital singlet ground state  $(e_g'^1a_{1g}^1)$ . In the strong crystal field basis, the doublet state corresponds to the  $d_{xy}, d_{yz}$  orbitals, while the singlet arises from the  $d_{z^2}$  orbital.

The high resolution RIXS spectra with multiple spectral features enabled a precise determination of the trig-

onal distortion parameter  $\Delta_{D_{3d}}$ . The obtained  $\Delta_{D_{3d}}$  in VI<sub>3</sub> (0.07 eV) is consistent with previous reports, while our study provides the first experimental determination of  $\Delta_{D_{3d}}$  in VBr<sub>3</sub> (-0.096 eV) [37, 38]. These findings confirm the critical role of the trigonal distortion in defining the electronic ground states in VX<sub>3</sub>. Although our results establish strong experimental evidence for the distinct electronic configurations, further investigations are warranted to quantitatively assess the SOC induced splitting within the  $e'_g$  manifold and its contribution to the Mott insulating behavior in VI<sub>3</sub>.

#### VI. CONCLUSIONS

We have investigated the electronic structure and ground state configurations of vanadium trihalides  $VX_3$ (X = Br and I) using high resolution RIXS measurements combined with ligand field multiplet calculations. The RIXS spectra revealed distinct dd and charge-transfer excitations, enabling precise determination of the crystal field and electronic interaction parameters. From the multiplet simulations, we obtained crystal field splitting energies of 10Dq = 1.370 eV for VBr<sub>3</sub> and 1.220 eV for  $VI_3$ , with Racah parameters B = 0.057/0.050 eV and C = 0.423 eV, respectively. These values show a systematic reduction in crystal field strength and enhanced covalency as the halogen changes from Br to I. Our analysis established a high-spin  $V^{3+}$  (S=1) configuration with an  $e_g^{\prime 2}$  ground state in VBr<sub>3</sub> and an  $e_g^{\prime 1}a_{1g}^1$  ground state in VI<sub>3</sub>, corresponding to trigonal elongation and compression, respectively. The experimentally extracted parameters are in excellent agreement with theoretical and optical studies, providing the most complete experimental picture of the low-energy electronic structure in  $VX_3$  to date. These findings not only resolve long-standing ambiguities regarding the ground-state configurations of  $VX_3$  but also highlight the critical roles of SOC and ligand field tuning in defining their magnetic and transport properties. The precise energy scales reported here form a solid foundation for future theoretical modeling and offer key insights for designing next-generation spintronic and quantum materials based on layered vanadium halides.

#### ACKNOWLEDGMENTS

This research was conducted at PEAXIS RIXS beamline, BESSY II, Germany operated by the Helmholtz-Zentrum Berlin für Materialien und Energie and qRIXS 8.0.1 beamline, Advanced Light Source (ALS), which is a DOE Office of Science User Facility under contract no. DE-AC02-05CH11231. The Welch Foundation (grant number: E-0001) and the Texas Center for Superconductivity (TCSUH) supported work at the University of Houston. Part of this work was supported by the U.S. DOE, BES, under Award No. DE-SC0024332. The authors acknowledge support from the U.S. Air Force Office of Scientific Research and Clarkson Aerospace Corp. under Award FA9550-21-1-0460. Y.C.S. acknowledges the financial support from the National Science and Technology Council (NSTC) in Taiwan under grant numbers 113-2112-M-213-025-MY3. Special thanks to the eXn group members at the University of Houston.

# Appendix A: Determination of trigonal distortion parameter $\Delta_{D_{3d}}$

Under an  $O_h$  crystal field, the V 5d orbitals are split into two energy levels  $e_g$  and  $t_{2g}$ . The JT distortion under  $D_{3d}$  symmetry further splits the  $t_{2g}$  orbitals into  $a_{1g}$  and  $e_g'$  states. The local V symmetry used in the simulations was  $D_{3d}$ , which is reduced to  $C_3$  when the magnetic moment is added by  $(H_z = 1.9 \text{ meV for VBr}_3 \text{ and } H_z = 15.9 \text{ meV for VI}_3)$  [12, 16]. We can express the energy of each orbital as,

$$E(e_q) = 6Dq (A1a)$$

$$E(a_{1g}) = -4Dq - 2\Delta_{D_{3d}}$$
 (A1b)

$$E(e_q') = -4Dq + \Delta_{D_{3d}} \tag{A1c}$$

where  $\Delta_{D_{3d}}$  is the trigonal distortion parameter.

Figure 8 shows the ELD calculated as a function of  $\Delta_{D_{3d}}$  in (a) VBr<sub>3</sub> and (b) VI<sub>3</sub>. In order to determine the trigonal distortion parameter  $\Delta_{D_{3d}}$ , the region I in experimental RIXS data was fitted with five Gaussian peaks: two peaks for triplet states  $^3E$  and  $^3A_1$ , and three peaks for singlet states  $^1E$ ,  $^1A_2$ , and  $^1E$  states. The peak separation  $|^3E - ^3A_1|$  was determined to be 0.108 eV and 0.131 eV in VBr<sub>3</sub> and VI<sub>3</sub>, respectively. Considering this

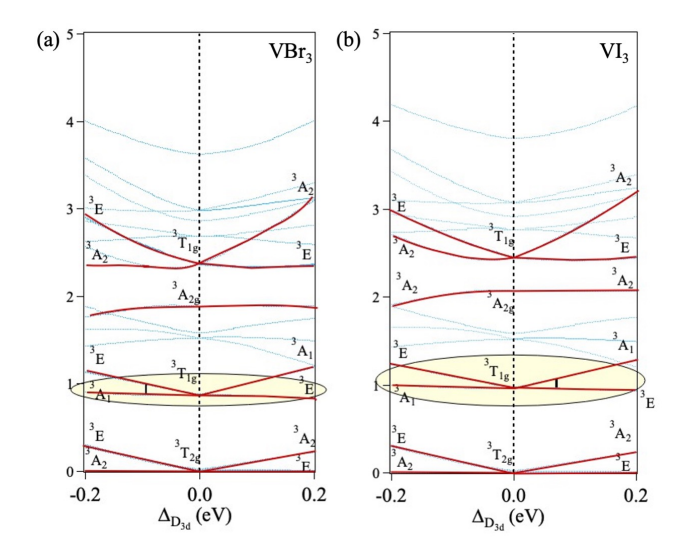


FIG. 8. Energy level diagram as a function of trigonal distortion parameter  $\Delta_{D_{3d}}$  in (a) VBr<sub>3</sub> and (b) VI<sub>3</sub>

energy gap along with the shoulder feature ordering in the two systems, the trigonal distortion parameters were determined to be -0.096 eV and 0.070 in VBr<sub>3</sub> and VI<sub>3</sub>, respectively.

#### **BIBLIOGRAPHY**

- Dahlia R Klein, David MacNeill, Jose L Lado, David Soriano, Efrén Navarro-Moratalla, Kenji Watanabe, Takashi Taniguchi, Soham Manni, Paul Canfield, Joaquín Fernández-Rossier, et al. Probing magnetism in 2D van der Waals crystalline insulators via electron tunneling. Science, 360(6394):1218–1222, 2018.
- [2] Shengwei Jiang, Lizhong Li, Zefang Wang, Kin Fai Mak, and Jie Shan. Controlling magnetism in 2D CrI<sub>3</sub> by electrostatic doping. *Nature nanotechnology*, 13(7):549–553, 2018.
- [3] Azkar Saeed Ahmad, Yongcheng Liang, Mingdong Dong, Xuefeng Zhou, Leiming Fang, Yuanhua Xia, Jianhong Dai, Xiaozhi Yan, Xiaohui Yu, Junfeng Dai, et al. Pressure-driven switching of magnetism in layered CrCl<sub>3</sub>. Nanoscale, 12(45):22935–22944, 2020.
- [4] Prakash Mishra and Tunna Baruah. Magnetic properties of CrX<sub>3</sub> (X= Cl, Br, I) monolayers in excited states. Journal of Materials Chemistry C, 12:5216-5221, 2024.
- [5] Tai Kong, Shu Guo, Danrui Ni, and Robert J Cava. Crystal structure and magnetic properties of the layered van der Waals compound VBr<sub>3</sub>. Physical Review Materials, 3(8):084419, 2019.
- [6] Junjie He, Shuangying Ma, Pengbo Lyu, and Petr Nachtigall. Unusual Dirac half-metallicity with intrinsic ferromagnetism in vanadium trihalide monolayers. *Journal of Materials Chemistry C*, 4(13):2518–2526, 2016.
- [7] Roberto Sant, Alessandro De Vita, Vincent Polewczyk, Gian Marco Pierantozzi, Federico Mazzola, Giovanni Vinai, Gerrit van der Laan, Giancarlo Panaccione, and NB Brookes. Anisotropic hybridization probed by polarization dependent x-ray absorption spectroscopy in VI<sub>3</sub>

- van der Waals Mott ferromagnet. Journal of Physics: Condensed Matter, 35(40):405601, 2023.
- [8] Lu Liu, Ke Yang, Guangyu Wang, and Hua Wu. Twodimensional ferromagnetic semiconductor VBr<sub>3</sub> with tunable anisotropy. *Journal of Materials Chemistry C*, 8(42):14782–14788, 2020.
- [9] Tai Kong, Karoline Stolze, Erik I Timmons, Jing Tao, Danrui Ni, Shu Guo, Zoë Yang, Ruslan Prozorov, and Robert J Cava. VI<sub>3</sub>—a new layered ferromagnetic semiconductor. Advanced Materials, 31(17):1808074, 2019.
- [10] BingBing Lyu, Le Wang, YiFan Gao, Shu Guo, Xuefeng Zhou, Zhanyang Hao, Shanmin Wang, Yue Zhao, Li Huang, Jifeng Shao, et al. Structural and magnetic phase transitions in quasi-two-dimensional VBr<sub>3</sub>. Physical Review B, 106(8):085430, 2022.
- [11] Shangjie Tian, Jian-Feng Zhang, Chenghe Li, Tianping Ying, Shiyan Li, Xiao Zhang, Kai Liu, and Hechang Lei. Ferromagnetic van der Waals crystal VI<sub>3</sub>. Journal of the American Chemical Society, 141(13):5326–5333, 2019.
- [12] Dávid Hovančík, Marie Kratochvílová, Tetiana Haidamak, Petr Doležal, Karel Carva, Anežka Bendová, Jan Prokleška, Petr Proschek, Martin Míšek, Denis I Gorbunov, et al. Robust intralayer antiferromagnetism and tricriticality in the van der Waals compound VBr<sub>3</sub>. Physical Review B, 108(10):104416, 2023.
- [13] Alexandru B Georgescu, Andrew J Millis, and James M Rondinelli. Trigonal symmetry breaking and its electronic effects in the two-dimensional dihalides MX<sub>2</sub> and trihalides MX<sub>3</sub>. Physical Review B, 105(24):245153, 2022.
- [14] Luigi Camerano and Gianni Profeta. Symmetry breaking in vanadium trihalides. 2D Materials, 11(2):025027, 2024.
- [15] Chamini S Pathiraja, Yi-De Chuang, Jayajeewana Niranjana Ranhili Pelige, Deniz Wong, Christian Schulz, Yu-Cheng Shao, Di-Jing Huang, Hsiao-Yu Huang, Amol Singh, and Byron Freelon. Spin-flip determination in crx 3 (x= cl, br, and i) 2d magnets using high-resolution x-ray scattering. In SMT 2025. APS, 2025.
- [16] Ke Yang, Fengren Fan, Hongbo Wang, DI Khomskii, and Hua Wu. VI<sub>3</sub>: A two-dimensional Ising ferromagnet. Physical Review B, 101(10):100402, 2020.
- [17] Alessandro De Vita, Thao Thi Phuong Nguyen, Roberto Sant, Gian Marco Pierantozzi, Danila Amoroso, Chiara Bigi, Vincent Polewczyk, Giovanni Vinai, Loi T Nguyen, Tai Kong, et al. Influence of orbital character on the ground state electronic properties in the van der Waals transition metal iodides VI<sub>3</sub> and CrI<sub>3</sub>. Nano letters, 22(17):7034-7041, 2022.
- [18] Xiaosong Zhao and Yukai An. Multiple Topological Phases with Electronic Correlation in Intrinsic Ferromagnetic Semimetal VI<sub>3</sub> Monolayer. Small, 20(50):2407232, 2024.
- [19] Suhan Son, Matthew J Coak, Nahyun Lee, Jonghyeon Kim, Tae Yun Kim, Hayrullo Hamidov, Hwanbeom Cho, Cheng Liu, David M Jarvis, Philip AC Brown, et al. Bulk properties of the van der Waals hard ferromagnet VI<sub>3</sub>. Physical Review B, 99(4):041402, 2019.
- [20] Luuk JP Ament, Michel Van Veenendaal, Thomas P Devereaux, John P Hill, and Jeroen Van Den Brink. Resonant inelastic x-ray scattering studies of elementary excitations. Reviews of Modern Physics, 83(2):705-767, 2011.
- [21] Chamini Pathiraja, Jayajeewana N Ranhili, Deniz Wong, Christian Schulz, Yi-De Chuang, Yu-Cheng Shao, Di-Jing Huang, Hsiao-Yu Huang, Amol Singh, and Byron

- Freelon. Electronic Energy Scales of  $CrX_3$  (X = Cl, Br, and I) using High-resolution X-ray Scattering. arXiv preprint arXiv:2504.04053, 2025.
- [22] Chamini S. Pathiraja, Jayajeewana N. Ranhili, Deniz Wong, Christian Schulz, Yi-De Chuang, Yu-Cheng Shao, Di-Jing Huang, Hsiao-Yu Huang, Amol Singh, and Byron Freelon. Electronic energy scales of  $\operatorname{crx}_3$  ( $x=\operatorname{cl},\operatorname{br},$  and i) using high-resolution x-ray scattering. *Phys. Rev. Res.*, 7:043139, Nov 2025.
- [23] Yi-De Chuang, Xuefei Feng, Alejandro Cruz, Kelly Hanzel, Adam Brown, Adrian Spucces, Alex Frano, Wei-Sheng Lee, Jaemyung Kim, Yu-Jen Chen, et al. Momentum-resolved resonant inelastic soft X-ray scattering (qRIXS) endstation at the ALS. Journal of Electron Spectroscopy and Related Phenomena, 257:146897, 2022.
- [24] Christian Schulz, Klaus Lieutenant, Jie Xiao, Tommy Hofmann, Deniz Wong, and Klaus Habicht. Characterization of the soft X-ray spectrometer PEAXIS at BESSY II. Journal of Synchrotron Radiation, 27(1):238–249, 2020.
- [25] YC Shao, B Karki, W Huang, X Feng, G Sumanasekera, J-H Guo, Y-D Chuang, and B Freelon. Spectroscopic determination of key energy scales for the base hamiltonian of chromium trihalides. *The journal of physical chemistry* letters, 12(1):724-731, 2021.
- [26] ML Farquhar, RA Wogelius, JM Charnock, P Wincott, CC Tang, M Newville, PJ Eng, and TP Trainor. Surface oxidation of rhodonite: structural and chemical study by surface scattering and glancing incidence XAS techniques. *Mineralogical Magazine*, 67(6):1205–1219, 2003.
- [27] Dmitry Ruzmetov, Sanjaya D Senanayake, and Shriram Ramanathan. X-ray absorption spectroscopy of vanadium dioxide thin films across the phase-transition boundary. Physical Review B—Condensed Matter and Materials Physics, 75(19):195102, 2007.
- [28] CH Maule, JN Tothill, Paul Strange, and JA Wilson. An optical investigation into the  $3d^1$  and  $3d^2$  transitionmetal halides and oxyhalides, compounds near to delocalisation. Journal of Physics C: Solid State Physics, 21(11):2153, 1988.
- [29] Maurits W Haverkort. Quanty for core level spectroscopy-excitons, resonances and band excitations in time and frequency domain. In *Journal of Physics:* Conference Series, volume 712, page 012001. IOP Publishing, 2016.
- [30] MW Haverkort, M Zwierzycki, and OK Andersen. Multiplet ligand-field theory using Wannier orbitals. *Physical Review B*, 85(16):165113, 2012.
- [31] M Atanasov, CA Daul, and C Rauzy. A dft based ligand field theory. In Optical Spectra and Chemical Bonding in Inorganic Compounds: Special Volume dedicated to Professor Jørgensen I, pages 97–125. Springer, 2004.
- [32] RG Woolley. Ligand-field analysis of transition-metal complexes. *International Reviews in Physical Chemistry*, 6(2):93-141, 1987.
- [33] Myrtille OJY Hunault, Yoshihisa Harada, Jun Miyawaki, Jian Wang, Andries Meijerink, Frank MF De Groot, and Matti M Van Schooneveld. Direct observation of Cr<sup>3+</sup> 3d states in ruby: Toward experimental mechanistic evidence of metal chemistry. The Journal of Physical Chemistry A, 122(18):4399–4413, 2018.
- [34] Giulio Racah. Theory of complex spectra. I. Physical Review, 61(3-4):186, 1942.
- [35] Y Yekta, H Hadipour, E Sasioğlu, C Friedrich, SA Jafari,

- S Blügel, and I Mertig. Strength of effective Coulomb interaction in two-dimensional transition-metal halides  $MX_2$  and  $MX_3$  (M= Ti, V, Cr, Mn, Fe, Co, Ni; X= Cl, Br, I). Physical Review Materials, 5(3):034001, 2021.
- [36] J Krzystek, Adam T Fiedler, Jennifer J Sokol, Andrew Ozarowski, SA Zvyagin, Thomas C Brunold, Jeffrey R Long, Louis-Claude Brunel, and Joshua Telser. Pseudooctahedral complexes of vanadium (III): electronic structure investigation by magnetic and electronic spectroscopy. *Inorganic chemistry*, 43(18):5645–5658, 2004.
- [37] David Hovancik, Jiri Pospisil, Karel Carva, Vladimir Sechovsky, and Cinthia Piamonteze. Large orbital magnetic moment in VI<sub>3</sub>. Nano Letters, 23(4):1175–1180, 2023.
- [38] H Lane, E Pachoud, JA Rodriguez-Rivera, M Songvilay, Guangyong Xu, Peter M Gehring, JP Attfield, RA Ewings, and Christopher Stock. Two-dimensional ferromagnetic spin-orbital excitations in honeycomb VI<sub>3</sub>. Physical Review B, 104(2):L020411, 2021.
- [39] Mandeep Dalal. A Textbook of Inorganic Chemistry– Volume 1. Dalal Institute, 2017.
- [40] Chamini Pathiraja, Jayajeewana Niranjana Ranhili Pelige, Yi-De Chuang, Deniz Wong, Christian Schulz, Yu-Cheng Shao, Di-Jing Huang, Hsiao-Yu Huang, and Byron Freelon. Determination of electronic

- structure parameters for different halides in crx 3 (x= cl, br, and i) using high-resolution x-ray scattering. Bulletin of the American Physical Society, 2025.
- [41] Andrei L Tchougréeff and Richard Dronskowski. Nephelauxetic effect revisited. *International Journal of Quantum Chemistry*, 109(11):2606–2621, 2009.
- [42] Mihail Atanasov, Dmitry Ganyushin, Kantharuban Sivalingam, and Frank Neese. A modern first-principles view on ligand field theory through the eyes of correlated multireference wavefunctions. *Molecular electronic* structures of transition metal complexes II, pages 149– 220, 2012.
- [43] Keisuke Tomiyasu, Jun Okamoto, Hsiao-Yu Huang, Zhi-Ying Chen, Evelyn Pratami Sinaga, Wen-Bin Wu, Yen-Yi Chu, Amol Singh, R-P Wang, FMF De Groot, et al. Coulomb correlations intertwined with spin and orbital excitations in LaCoO<sub>3</sub>. Physical Review Letters, 119(19):196402, 2017.
- [44] Vladimir I Anisimov, Ferdi Aryasetiawan, and AI Lichtenstein. First-principles calculations of the electronic structure and spectra of strongly correlated systems: the lda+ u method. *Journal of Physics: Condensed Matter*, 9(4):767, 1997.